RESEARCH PAPER

A quasi-continuum multi-scale theory for self-diffusion and fluid ordering in nanochannel flows

Antonios E. Giannakopoulos · Filippos Sofos ·
Theodoros E. Karakasidis · Antonios Liakopoulos

Abstract We present a quasi-continuum self-diffusion theory that can capture the ordering effects and the density variations that are predicted by non-equilibrium molecular dynamics (NEMD) in nanochannel flows. A number of properties that affect fluid ordering in NEMD simulations are extracted and compared with the quasi-continuum predictions. The proposed diffusion equation requires the classic diffusion coefficient D and a micro structural internal length g that relates directly to the shape of the molecular potential of the NEMD calculations. The quasi-continuum self-diffusion theory comes as an alternative to atomistic simulation, bridging the gap between continuum and atomistic behavior with classical hydrodynamic relations and reduces the computational burden as compared with fully atomistic simulations.

List of symbols

A_{1-4}	Constants determined by BC
A, B	Constants for inhomogeneous diffusion
A_i, B_i	Airy functions
c	Concentration
c_{1-3}	Real constants
D	Bulk diffusion coefficient
D_{ap}	Apparent diffusion coefficient
F	Diffusion functional
F_{ap}	Apparent diffusion functional
$_1F_1$	Hypergeometric function
F_{ext}	Magnitude of external driving force
g	Wavelength
G	Gibbs free energy
G_0	Gibbs free energy at equilibrium
h	Boundary value for concentration
H	Hermitian polyomial
h_{ch}	Channel height
$\underline{J}$	Diffusional flux
$\underline{K}$	Gradient energy coefficient
K^*	Spring constant
L_x	Length of the computational domain in the x-direction
L_y	Length of the computational domain in the y-direction
L_z	Length of the computational domain in the z-direction
M	Diffusional mobility
n	Integer number, $n = 0, 1, 2…$
p	Pressure
q	Boundary value for the non-classic flux term
r_{eq}	Position of a wall atom on fcc lattice site
$\mathbf{r}_i$	Position vector of atom i
$\mathbf{r}_{ij}$	Distance vector between ith and jth atom
T	Temperature
S	Area
$u(r_{ij})$	LJ potential of atom i with atom j
V	Volume
w	Boundary condition for the normal flux
z^*	Normalized distances in the z-direction

Greek letters

ε	Energy parameter in the LJ potential
μ	Local chemical potential

A. E. Giannakopoulos · F. Sofos · T. E. Karakasidis (✉) ·
A. Liakopoulos
Department of Civil Engineering, School of Engineering,
University of Thessaly, 38834 Pedion Areos, Volos, Greece
e-mail: thkarak@uth.gr

ρ Fluid density
σ Length parameter in the LJ potential

1 Introduction

Nanofluidics has emerged as an important subfield of nanotechnology with important applications in biomedical science where minute amount of fluids move through microtubules. Drug delivery investigations stand to profit enormously from studies of nanochannel flows. For such flows, non-equilibrium molecular dynamics (NEMD) offers an effective simulation method, as has been recently undertaken by many researchers (Binder et al. 2004; Hartkamp et al. 2012; Sofos et al. 2009a, b; Li and Liu 2012). Within this framework, simulation of planar Poiseuille flow in a channel offers the best way of establishing the range of applicability of continuum-based theories. Density profiles reveal strong oscillations in the number of fluid atoms at layers adjacent to the walls. This inhomogeneity in the fluid concentration in the channel cannot be explained by the classical diffusion theory. Nanofluidics is not the only field where ordering of the mater takes place. Magnetization, martensitic transformation and dislocations also show ordering of mater (Stanley 1971).

Somers and Davis (1991) presented an early full analysis of density profiles for channel widths from 0.6 to 2.35 nm. They observed that fluid atoms are ordered in distinct layers, symmetrical with respect to the midplane of the channel. These layers are not affected by the magnitude of the external driving force (Nagayama and Cheng 2004). The fluid density peak values decreases as temperature increases. The stiffness of the walls affects the fluid ordering for channels of very small widths (Priezjev 2007). Average fluid density also affects fluid ordering in a significant way. Iwai et al. (1996) performed Monte Carlo calculations and showed variation in the radial distribution function of supercritical carbon dioxide around OH groups of xylenol isomers at 308.15 K and 13 MPa.

In the present paper, we will develop a new quasi-continuum self-diffusion theory that can capture the ordering effects and the density variations that are predicted by non-equilibrium molecular dynamics (NEMD) in nanochannel flows from Sofos et al. (2009a). A new diffusion equation is proposed, together with new boundary conditions. The solution of the new diffusion equation provides a better approximation to the density variations. The flux constitutive equation requires the classic self-diffusion coefficient, D, and, in addition, a micro structural internal length, g, that relates directly to the shape of the molecular potential that is used in the NEMD calculations. There are

several benefits for choosing a quasi-continuum self-diffusion theory instead of NEMD. Aside from the smaller computational cost, the quasi-continuum theory can easily describe complex two and three dimensional domains, include various boundary conditions and incorporate convective terms, if combined with other classic hydrodynamic numerical schemes.

1.1 A quasi-continuum theory of diffusion in fluids

Diffusional flux $\underline{J}$ is spontaneous and leads to the decrease in the Gibbs free energy G of a non-reacting fluid. Note that we use G in case of constant temperature, as in the examples that we will study. Our analysis has some similarities with the spinodal decomposition of a binary solid system (Cahn and Hilliard 1958); however, the present theory is not the same.

The basic constitutive equation concerns the driving force for diffusion and is taken as the gradient of the local chemical potential μ (Darken 1948):

$$\underline{J} = -M\underline{\nabla}\mu \tag{1}$$

where M is the diffusional mobility and is positive. The above relation implies isotropy (true for most fluids) and reminds Ohm's law of electric conductivity. Eq. (1) implies that we will ignore the effect of the Brownian motion. Cook (1970) included the influence of the thermal fluctuations, adding the gradient of a fluctuating field.

In the absence of an external field (e.g., gravity), the local chemical potential is related to the free energy density as[1]

$$\mu = \frac{\partial G}{\partial c} \tag{2}$$

at constant pressure ($p = $ const) and temperature ($T = $ const). G is the free energy per unit molecule volume, and we can express it as (Cahn and Hilliard 1959)

$$G = G_o(c) + K(\underline{\nabla}c)^2 \tag{3}$$

where c is the concentration ($c = c(\underline{x}, t)$ is a function of position $\underline{x}$ and time t,$[c] = $ [molecules/m^3]) and K is the gradient energy coefficient ($K > 0$). The energy term $K(\nabla c)^2$ is a measure of the increase in energy due to the non-uniform environment of atoms in a concentration gradient and implies a surface tension due to the gradient of the concentration. The constant K is approximately independent of composition and temperature. K depends on the number of molecules per unit volume, the critical temperature and the square of the intermolecular distance. Note that Eq. (3) implies that G changes from point to point

---

[1] If a gravitational field ϕ is present, we replace μ with $\mu + m\phi$ (m is the mass per mole). For $\phi = $ const, the present results will still hold true.

in the control volume of a fluid in thermodynamic equilibrium. In the equations, ∇^2 is the Laplacian operator ($\nabla^2 = \partial^2/\partial x_1^2 + \partial^2/\partial x_2^2 + \partial^2/\partial x_3^2$, for Cartesian coordinates) and ∇ is the gradient vector ($\nabla = \{\partial/\partial x_1, \partial/\partial x_2, \partial/\partial x_3\}$, for Cartesian coordinates).

Combining Eqs. (2) and (3), we obtain

$$\mu = \frac{\partial G_o}{\partial c} + 2K\nabla^2 c \tag{4}$$

Then, the Fick's 2nd law can be found from Eqs. (1) and (4)

$$\underline{J} = -M\left\{\frac{\partial^2 G_o}{\partial c^2}\underline{\nabla}c + 2K\underline{\nabla}(\nabla^2 c)\right\} \tag{5}$$

Define as the bulk diffusion D the positive quantity

$$D = M\frac{\partial^2 G_o}{\partial c^2} \tag{6}$$

Note that, if D is a fluid constant parameter, Eq. (6) implies that $\frac{\partial^2 G_o}{\partial c^2}$ is a positive constant. Therefore,

$$\underline{J} = -D\left\{\underline{\nabla}c + \frac{2MK}{D}\underline{\nabla}(\nabla^2 c)\right\} \tag{7}$$

is the new 1st Fick's law. In the case where $\nabla^2 c \approx$ const, or for $K \approx 0$, we obtain the classic Fick's law

$$\underline{J}_{\text{classic}} = -D\underline{\nabla}c \tag{8}$$

Taking the conservation of mass, in the absence of convective (flow) and source (reactions, radiation, etc.) terms:

$$\frac{\partial c}{\partial t} = -\underline{\nabla}J \tag{9}$$

Combining Eqs. (7) and (9), we obtain the augmented 2nd Fick's law

$$\frac{\partial c}{\partial t} = D\nabla^2 c + 2MK\nabla^4 c \tag{10}$$

Note that the constant

$$g^2 = \frac{2KM}{D} \tag{11}$$

has dimensions $[g^2] = [L^2]$. This will provide a dominant wave length of order g and a wave number $2\pi/g$. Therefore, for $t \geq 0$,

$$\frac{\partial c}{\partial t} = D\{\nabla^2 c + g^2\nabla^4 c\} \tag{12}$$

We again observe that in case $\nabla^2 c \approx$ const or $K \approx 0$, we obtain the classic 2nd Fick's law

$$\left.\frac{\partial c}{\partial t}\right|_{\text{classic}} = D\nabla^2 c \tag{13}$$

Equation 12 describes a quasi-continuum theory of self-diffusion and can be solved provided we describe appropriate initial and boundary condition.

The Cahn–Hilliard spinodal decomposition diffusion law (Cahn 1961) uses the integral form of Eq. (3) as a total free energy functional, leading to a negative diffusion coefficient D and a similar form with Eq. (12).

1.2 Initial and boundary conditions

In order to solve Eq. (12) with respect to the concentration c as a function of the coordinates $\underline{z}$ and the time t, we need to establish initial conditions at a certain time $t = t_*$

$$c_*(\underline{z}) = c(\underline{z}, t_*) \tag{14}$$

To establish boundary conditions, we formulate the steady state version of Eq. (12)

$$D(\nabla^2 c - g^2\nabla^4 c) = 0 \tag{15}$$

We construct a functional F of the form

$$F(\nabla^2 c) = \frac{D}{2}\iiint\limits_V (\nabla^2 c)(\nabla^2 c + g^2\nabla^4 c)\mathrm{d}V \tag{16}$$

With the volume integral covering the volume V of the fluid that diffusion takes place. Using Green's theorem (Courant and Hilbert 1953)

$$\frac{2}{D}F(\nabla^2 c) = \iiint\limits_V \left\{(\nabla^2 c)^2 - g^2\underline{\nabla}(\nabla^2 c) \cdot \underline{\nabla}(\nabla^2 c)\right\}\mathrm{d}V$$
$$+ g^2\iint\limits_{\partial v} (\nabla^2 c)(\underline{\nabla}(\nabla^2 c) \cdot \underline{n})\mathrm{d}S \tag{17}$$

where $\underline{n}$ is the outer unit normal vector to the boundary surface ∂V of the volume V. We can then immediately observe the boundary condition (BC):

$$g^2\underline{\nabla}(\nabla^2 c) \cdot \underline{n} = q \quad \text{on} \quad \partial V \tag{18}$$

The functions F and q will be considered as known functions of $\underline{z} \in \partial V$ (surface coordinates) and of $t \geq t_o$ (time).

From the BC (18) and the variation of $F(\nabla^2 c)$ with respect to $\nabla^2 c$, we obtain the Euler–Lagrange equation which is exactly as the steady state Eq. (15). In order to have minimum for $F(\nabla^2 c)$, we must have the additional Legendre condition

$$(\nabla^2 c)^2 - g^2\underline{\nabla}(\nabla^2 c) \cdot \underline{\nabla}(\nabla^2 c) \geq 0 \tag{19}$$

In addition to the non-classic BC (18), we have the classic BC:

$$c = h \quad \text{or} \quad \underline{\nabla}c \cdot n = f \quad \text{on} \quad \partial V \tag{20}$$

From Eq. (20), we also combine the non-classic BC in the form that is physically meaningful

$$\underline{n} \cdot \underline{J}(\underline{z}, t) = -D\{\underline{\nabla}c + g^2 \underline{\nabla}(\nabla^2 c)\} \cdot \underline{n} = -D(f + q) = w$$
$$\text{on} \quad \partial V \tag{21}$$

where h and w are known functions of $\underline{z} \in \partial V$ (surface points) and of time $t \geq t_o$.

Note that the BC (21) reflects directly to the chemical potential at the boundary (Eq. (1)), which also relates to the roughness of the boundary walls (Priezjev 2007) and to the hydrophilic/hydrophobic wall–fluid interaction (Voronov et al. 2006). Wetting condition could correspond to $\nabla c \cdot n = 0$, so $q = 0$ in Eq. (18). Local conservation of mass supposes that $w = 0$ and combined with $q = 0$ gives $f = 0$.

Suppose that an apparent diffusion coefficient D_{ap} can be related to the classic diffusion equation as

$$\frac{\partial c}{\partial t} = D_{\text{ap}} \nabla^2 c \tag{22}$$

and the corresponding steady state equation

$$D_{\text{ap}} \nabla^2 c = 0 \tag{23}$$

We can construct a functional F_{ap}

$$F_{\text{ap}}(\nabla^2 c) = \frac{D_{\text{ap}}}{2} \iiint_V (\nabla^2 c)^2 dV \tag{24}$$

The minimization of F_{ap} leads to Eq. (23) (Crank 1975). In this case, we can use the BC from Eq. (20).

Using the enclosure theorem (Courant and Hilbert 1953) and the condition of Eq. (19), we have

$$\min F(\nabla^2 c) \geq \min F_{\text{ap}}(\nabla^2 c) \tag{25}$$

Using the minimization function $\nabla^2 c$ for both $F(\nabla^2 c)$ and $F_{ap}(\nabla^2 c)$, we obtain

$$\frac{D_{\text{ap}}}{D} \leq 1 - g^2 \frac{\int_V \underline{\nabla}(\nabla^2 c) \cdot \underline{\nabla}(\nabla^2 c) dV}{\int_V (\nabla^2 c)^2 dV} \leq 1 \tag{26}$$

This result states that the apparent diffusion constant D_{ap} is less than the "true" (intrinsic) bulk diffusion constant D.

Note that $F(\nabla^2 c)$ can be thought of as an evolutionary criterion toward the steady state, since the transient solution $\nabla^2 c$ (without convection) is an admissible function for the minimum of $F(\nabla^2 c)$ (Prigogine and Glansdorff 1965).

Let us formulate a restricted variational principle: Define the local potential

$$F(\nabla^2 c, \nabla^2 c_o)$$
$$= \int_0^t \iiint_V \left\{ \frac{D}{2} \left[(\nabla^2 c)^2 - g^2 \underline{\nabla}(\nabla^2 c) \cdot \underline{\nabla}(\nabla^2 c) \right] \right\}$$
$$\qquad\qquad - \nabla^2 c \frac{\partial c_o}{\partial t} \right\} dV \, dt \tag{27}$$

with known additional initial condition $\nabla^2 c(\underline{z}, t = 0) = 0$. We seek to make the local potential (Eq. 27) stationary with respect to variations in $\nabla^2 c$, holding c_o constant. After the variation, we set $c = c_o$ (c is the true solution) and we obtain

$$D(\nabla^2 c + g^2 \nabla^4 c) - \frac{\partial c}{\partial t} = 0 \tag{28}$$

and

$$g^2 \underline{\nabla}(\nabla^2 c) \cdot n = 0 \tag{29}$$

Clearly, Eq. (28) is the dynamic form of Fick's 2nd law and Eq. (28) provides the new boundary condition for the problem.

1.3 The 1D steady state example

It is instructive to solve the 1D steady state problem:

$$\frac{d^2 c}{dz^2} + g^2 \frac{d^4 c}{dz^4} = 0 \tag{30}$$

The solution of Eq. (30) is detailed in Appendix 1. We have

$$\frac{c}{c_o} = \frac{\frac{\bar{c}}{c_o} - \frac{2g}{h_{\text{ch}}} \sin \frac{h_{\text{ch}}}{2g}}{1 - \frac{2g}{h_{\text{ch}}} \sin \frac{h_{\text{ch}}}{2g}} + \frac{1 - \frac{\bar{c}}{c_o}}{1 - \frac{2g}{h_{\text{ch}}} \sin \frac{h_{\text{ch}}}{2g}} \cos \left(\frac{\frac{h_{\text{ch}}}{2} - z}{g} \right) \tag{31}$$

Note that for $h_{\text{ch}} \geq 2g$, $c(z)$ is positive for all z, provided that $\bar{c}/c_o \geq 1$.

If $\frac{g}{h} \to 0$, $A_1 \to \bar{c}$. For $c \geq 0$, for all z, $\frac{c}{c_o} \to \frac{\bar{c}}{c_o} \to 1$ and this is the classic solution ($c = \bar{c} = c_o$). In other words, as the channel becomes large compared to g, the classic solution is recovered. The result of Eq. (31) was found to be in agreement with the molecular dynamics results of Sofos et al. (2009a) with a dominant wavelength $g \approx 0.9\sigma$, where σ is the basic length that controls the Lennard-Jones potential ($\sigma = 0.3405$ nm for the Ar liquid used in our molecular dynamics computations).

2 The case of inhomogeneous diffusion mobility

In Sect. 2, we treated the diffusion D as a positive constant. However, this may not be true in cases of confinement of the fluid in thin channels or other devices. The solid walls usually decrease the diffusion close to the walls, but can under certain circumstances increase it:

$$D = D(z) > 0 \quad \underline{z} \in V \tag{32}$$

$$\max D(z) \text{ or } \min D(z) \quad \underline{z} \in \partial V \tag{33}$$

In this case, Eq. (11) describes a length that depends on $\underline{z}$
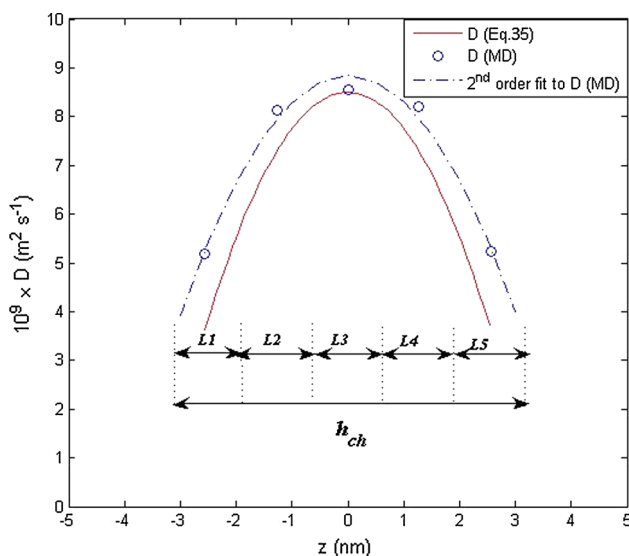
$$g = g(\underline{z}) \tag{34}$$

Fig. 1 Comparison of diffusion coefficient calculated from Eq. (35) with MD results, for an $h_{ch} = 6.4$ nm channel. MD values shown are taken from Sofos et al. (2009b) at $T = 150$ K and are fitted to a 2nd order polynomial

To fix ideas [as indicated by the molecular dynamics calculation in Sofos et al. (2009b)], let us take the steady state case in one dimension with the symmetric inhomogeneous diffusion distribution ($-h_{ch}/2 \leq z \leq h_{ch}/2$)

$$D = D_0\left(1 - A^2 z^2\right) \tag{35}$$

where D_0 the bulk diffusion and A constant with $1 \geq A^2 h_{ch}^2/4$. Molecular dynamics results confirm the above distribution for channels that have symmetric wall conditions. In Fig. 1, for an $h_{ch} = 18.58\sigma$ ($h_{ch} = 6.4$ nm) channel, we divide the channel in five layers (L1–L5), each one of width about 3.7σ and calculate the local average diffusion coefficient, in each layer. These results are then used to draw the 2nd order polynomial fit shown in Fig. 1. We observe a good agreement of calculated data to the proposed fit and, moreover, calculated local diffusion coefficient values seem to be in agreement with values obtained using Eq. (35). All the necessary diffusion coefficient values are taken from the molecular dynamics simulation results of Sofos et al. (2009b).

The particular form of Eq. (35) can be explained by a potential that incorporates the wall interactions to include wetting conditions (Marko 1993; Lipowsky and Fisher 1986; Lipowsky and Huse 1986).

Note that both A and D_0 depend on the channel size, where $-h_{ch}/2 \leq z \leq h_{ch}/2$. Clearly, as we approach the channel walls ($z = \pm h_{ch}/2$), diffusion decreases. Then

$$g^2 = \frac{2KM}{D_o\left(1 - A^2 z^2\right)} = \frac{g_o^2}{1 - A^2 z^2} \tag{36}$$

It must be recalled that $g_o < h_{ch}/2$. The diffusion Eq. (30) becomes

$$\frac{d^4 c}{dz^4} + \frac{1 - A^2 z^2}{g_o^2}\frac{d^2 c}{dz^2} = 0 \tag{37}$$

The solution of Eq. (37) is shown in Appendix 2. In a more general case, we can use the approximate method of Wentzel, Kramers and Brillouin (WKB) for solving the stationary Schrodinger's equation that resembles up to a sign Eq. (37). We can write

$$g^2 = g_o^2/P^2(z) \tag{38}$$

Then the approximate solution of Eq. (37) becomes

$$\frac{d^2 c}{dz^2} \approx \frac{c_1}{\sqrt{P}}\sin\left(\frac{1}{g_o}\int P(z)dz + c_2\right) \tag{39}$$

For $P(z) = (1 - A^2 z^2)^{1/2}$

$$\int P(z)dz = \frac{z}{2}\sqrt{1 - A^2 z^2} + \frac{\arcsin(Az)}{2A} \tag{40}$$

A "quantum" condition can be stated by observing that an increase in phase $\frac{1}{g_o}\int P dz + c_2$ in a complete rotation would have to be an integer multiple of 2π. Let the boundaries $z = \pm h_{ch}/2$ be the two turning points. Then

$$\int_{-h_{ch}/2}^{h_{ch}/2} P(z)dz = 2n\pi g_o, \quad n = 0, 1, 2, \ldots \tag{41}$$

In the present example, Eq. (40) gives

$$\left(\sqrt{1 - A^2\left(\frac{h_{ch}}{2}\right)^2} + \frac{\arcsin(A\, h_{ch}/2)}{A\, h_{ch}/2}\right) = 2\pi\frac{2g_o}{h_{ch}}n \tag{42}$$

If we know any two of h_{ch}, g_o and A, we can estimate the third one, provided we can estimate the integer n ($A \neq 0$ in this case).

For the case of asymmetric wall conditions, refer to Appendix 3.

3 Molecular system modeling

3.1 System details

The flow system simulated by non-equilibrium molecular dynamics (NEMD) is consisted of two infinite plates with argon flowing between them (equivalent to Poiseuille flow), as shown in Fig. 2. The LJ potential is used here:

$$u^{LJ}(r_{ij}) = 4\varepsilon\left(\left(\sigma/r_{ij}\right)^{1/2} - \left(\sigma/r_{ij}\right)^{6}\right) \tag{43}$$

where, for liquid argon, we employ $\sigma = 0.3405$ nm, $\varepsilon_{fluid}/k_B = 119.8$ K, cutoff radius for the potential $r_c = 2.5\sigma$,
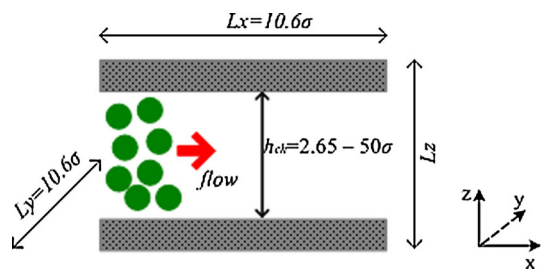
Fig. 2 The MD system under examination

constant mean fluid density ($\rho = 1{,}078$ kg/m^3, or $\rho^* = 0.642\sigma^{-3}$).

MD simulation is performed in a simulation window of ($L_x \times L_y \times L_z$) dimensions. Periodic boundary conditions are used along the x- and y-directions, while the distance between the two plates in the z-direction corresponds to the channel width, h_{ch}. In this way, we construct a Poiseuille flow system, with two infinite plates in the xy-plane, separated by a distance h_{ch}. Based on the fundamental formulation of MD (e.g., Allen and Tildesley 1987), due to periodic boundary conditions, each particle that exits the simulation window on the right enters the channel form the left, while particles approaching the walls are bounced back toward the interior of the channel.

An external force F_{ext} is applied to the x-direction to every fluid particle to drive the flow. Wall atoms are kept bound around their original fcc lattice positions by an elastic string force $\mathbf{F} = -K^*(\mathbf{r}(t) - r_{eq})$, where $\mathbf{r}(t)$ is the position vector of an atom at time t, r_{eq} is its initial lattice position vector, and $K^* = 57.15(\varepsilon/\sigma^2)$ is the spring constant.

Wall atoms absorb the increase in kinetic energy of the fluid atoms, which is caused by the application of the external force, and Nose–Hoover thermostats are applied at the thermal walls in order to keep the system's temperature constant (Sofos et al. 2009a; Evans and Holian 1985; Holian and Voter 1995). We employ two independent thermostats one for the upper wall and another for the lower wall in order to achieve better thermalization of the wall atoms (see Appendix 4 for details). More details on system parameters can be found in Sofos et al. (2009b).

The NEMD computed self-diffusion coefficient for liquid argon compares with the macroscopic measurements as suggested by the present approach. For $T = 100$ K, Sofos et al. (2009b) computed a self-diffusion coefficient $D = 5 \times 10^{-5}$ cm^2/s. Experiments of Gini-Constagnoli and Ricci (1960) give $D = 1.53 \times 10^{-5}$ cm^2/s for $T = 84.56$ K. Using molecular dynamics, Thomas and McGaughey (2007) report $D = 4.03 \times 10^{-5}$ cm^2/s for $T = 90$ K.

3.2 Density profiles

In order to calculate values that consist the density profile, the nanochannel was partitioned in m computational domains (bins) along the z-direction, each of volume $V_{bin} = L_x L_y h_{bin}$, where $h_{bin} = h_{ch}/m$. At each time instant, the density of the liquid $N^*(z)$ is the number of atoms located inside each bin. The number of atoms is calculated during the whole time of the calculations and the average is

$$N(z) = \frac{\langle N_{bin}(z, z + h_{bin})\rangle}{N_f} \qquad (44)$$

To check the molecular dynamic model (LJ potential), the cutoff radius r_c was allowed to take the values 2.5σ, 3σ and 3.5σ. Minor influence was observed to the results (an increase in r_c reduces slightly the peaks of the calculated density distributions).

We examine the effect of temperature, T, on the density profile presented in Fig. 3a. For $h_{ch} = 2.65\sigma$ (or, $h_{ch} = 0.9$ nm), we observe that fluid atoms are ordered in two distinct layers, symmetrical with respect to the channel mid-plane. The fluid density peak value decreases as temperature increases. Similar ordering in the fluid has been reported in Somers and Davis (1991) for $h_{ch} = 2.5\sigma$ and 2.75σ. Although the peaks magnitude decreases, there is a clear periodicity for their appearance at about 0.9σ, as shown in Fig. 3a. This trend remains in all density profiles presented in this study, for all channel widths. The effect of the magnitude of the external applied force, F_{ext}, to density profiles is negligible, at least in the range examined here (Fig. 3b). This is in agreement with the results reported in Nagayama and Cheng (2004). We remind that the force range studied here does not result in system non-linearities (Binder et al. 2004).

In Fig. 3c we investigate the effect of channel width, h_{ch}, on the density profile. In small channels ($2\sigma \leq h_{ch} \leq 8\sigma$) the strong influence of the walls extends over all or most of the fluid atoms and this fact results in oscillations on the density profile. It is clear that as h_{ch} increases ($10\sigma \leq h_{ch} \leq 20\sigma$) homogeneity is induced in the interior of the channel, while there is always a region of fluid non-homogeneity region becomes non-significant, i.e., for $h_{ch} \approx 20\sigma$ the non-homogeneity region is less than 10 % of the available channel width.

The wall spring constant K^* is an indication of wall atoms stiffness (Asproulis and Drikakis 2011), i.e., the walls become stiffer when K^* value is greater. In the diagram of Fig. 3d, we observe that density peaks are broader and of smaller amplitude as K^* decreases, as also found in Priezjev (2007), and we attribute this to the fact that, for smaller K^* values, wall atoms oscillate more and fluid atoms are more possible to localize closer to the walls.
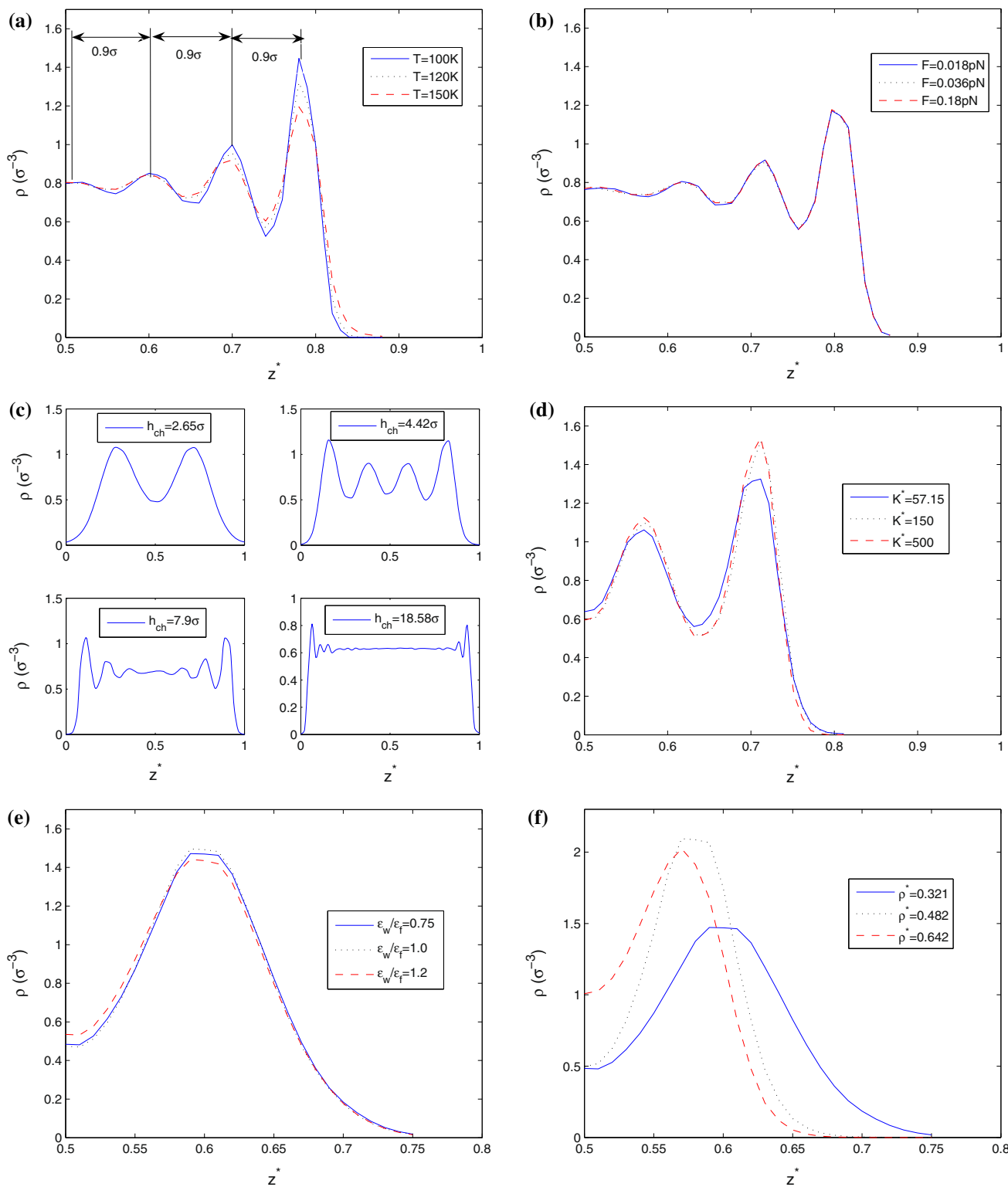
Fig. 3 Density profiles extracted from MD model, shown from channel middlepoint to the wall (symmetric channels) **a** for various T ($h_{ch} = 7.9\sigma$), **b** for various magnitudes of F_{ext} ($h_{ch} = 7.9\sigma$), **c** for various channel widths, **d** for various K^* values ($h_{ch} = 4.42\sigma$), **e** for various wall–fluid interaction values ($h_{ch} = 2.65\sigma$) and **f** various average fluid densities ($h_{ch} = 2.65\sigma$). For presentation reasons, since we refer to channels of various width, we normalized z-direction to $0 \leq z^* \leq 1$

We examine the effect of various wall–fluid interactions $\varepsilon_w/\varepsilon_f$ on density profile in Fig. 3e. As the ratio $\varepsilon_w/\varepsilon_f$ increases, fluid atoms are attracted to the walls and wall surface becomes hydrophilic, while as $\varepsilon_w/\varepsilon_f$ decreases, fluid atoms are less attracted to the walls and wall surface becomes hydrophilic (Voronov et al. 2006). This approach was also used in Sofos et al. (2012), where potential energy contours near the walls show that a large $\varepsilon_w/\varepsilon_f$ ratio leads in increased fluid atom presence near the walls (hydrophilic wall), while a small $\varepsilon_w/\varepsilon_f$ ratio leads in decreased fluid atom presence near the walls (hydrophobic wall). Wall wettability depends on the fluid contact angle on the surface, which, in turn, depends on the $\varepsilon_w/\varepsilon_f$ ratio (Voronov et al. 2006).

Average fluid density, ρ^* also affects fluid ordering in a significant way (Fig. 3f). We observe that as average fluid density decreases, the amplitudes of two peaks at the density profile increase significantly and fluid atoms are ordered near the walls, while strong inhomogeneity is induced.

Having studied all parameters (T, F_{ext}, K^*, $\varepsilon_{wall}/\varepsilon_{fluid}$ and ρ^*) for every channel width h_{ch} (we have examined all cases, but we do not present all diagrams here), we come to the conclusion that every parameter has a different impact on the density profile.

To sum up with results shown here, we first note that as system temperature increases, fluid ordering near the walls is decreased. This is attributed to increased fluid particle mobility in higher temperatures. As a result, an increase in system temperature leads to smoother density profiles. The flow is driven by a body force acting on all fluid particles equivalent to a pressure difference in Poiseuille flow. By changing the magnitude of the external force, we obtain no significant effect on fluid ordering near the walls. When the average fluid density decreases in the channels studied here, an increase of fluid inhomogeneity is observed. This can be attributed to the fact that for low density flows, particles are attracted by the wall atoms and tend to "stick" close to the walls, as they do not encounter strong attractive forces from other fluid atoms. For denser fluids, there is a significant number of fluid atoms in the channel that interact with each other and this fact helps them spread over the whole extend of the channel.

On the other hand, two properties that characterize the wall behavior, i.e., the wall spring constant K^* and the ratio $\varepsilon_{wall}/\varepsilon_{fluid}$, affect only channels of smaller widths ($h \leq 10\sigma$). For $h_{ch} \geq 10\sigma$, the effect of these two parameters extends only in a small region close to the walls (about 1–1.5σ) and is negligible in the remaining of the channel.

4 Comparison of the quasi-continuum theory with MD simulations

The molecular dynamics results (Sofos et al. 2009a) suggest that the parameter A in Eq. (35) is almost invariant
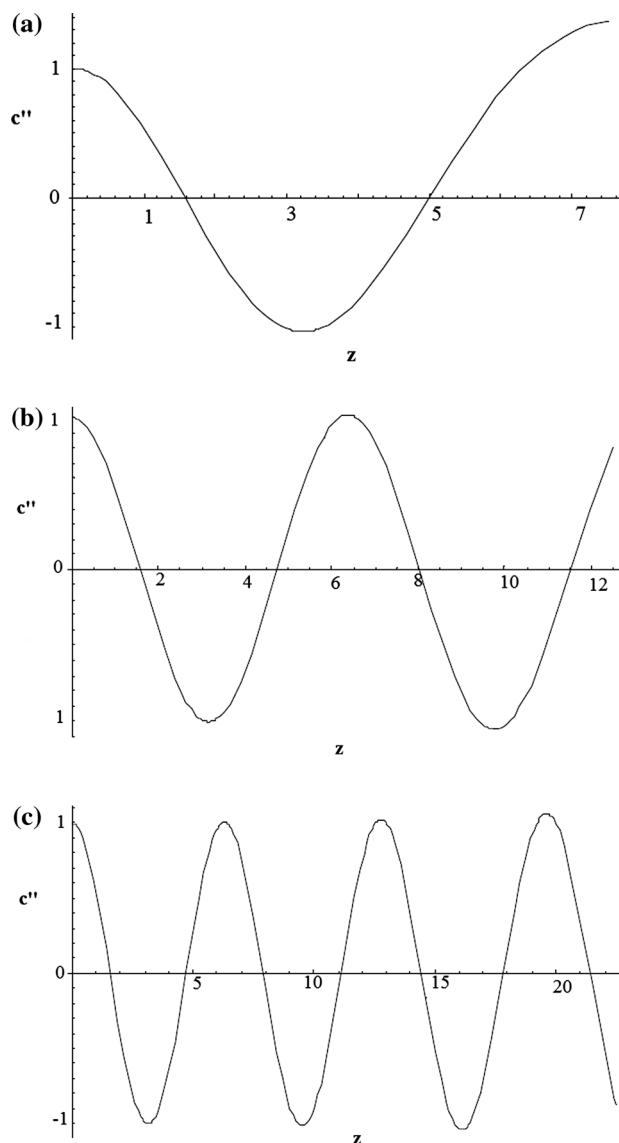

Fig. 4 Calculation of d^2c/dz^2 from Eq. (48). The values of Ag_o were fitted to minimize the difference with the molecular dynamic results of Fig. 3. The coordinate z scales with $0.2g_o (g_o = 0.3$ nm). **a** $Ag_o = 0.12$, $n = 1$ $(\frac{c''}{c_2} - \frac{z}{0.2g_o})$ and $h = 0.9$ nm **b** $Ag_0 = 0.045$, $n = 1$ $\left(\frac{c''}{c_2} - \frac{z}{0.2g_o}\right)$ and $h = 1.5$ nm **c** $Ag_0 = 0.024$, $n = 1$ $(\frac{c''}{c_2} - \frac{z}{0.2g_o})$ and $h = 2.7$ nm

with temperature T, but decreases to zero as the channel width h_{ch} increases. From the density profiles shown in Fig. 3a–f, it is clear that an oscillatory density profile appears that is exponentially decreasing from the walls to the interior of the channel. In all cases studied, a high density peak appears near the wall and consecutive peaks of smaller height appear as the profile approaches the middle of the channel. The exponential decay weakens as the channel width increases and saturates to constant fluid density at widths about $h_{ch} > 10\sigma$.

Table 1 Analysis of the molecular dynamic calculations by the quasi-continuum model

h_{ch}(nm)	Molecular dynamics		Quasi-continuum	
	g_o(nm)	A(nm^{-1})	$Ah_{ch}/2$	g_o(nm), Eq. (53)
0.9	0.3	0.6667	0.3000	0.141
1.5	0.3	0.2500	0.1875	0.237
2.7	0.3	0.1333	0.1800	0.427

It is also of great interest to keep in mind that the oscillation periodicity gives an almost constant wavelength of about 0.9σ (≈ 0.3 nm in the argon case), as shown in Fig. 3a. This wavelength is constant, no matter what property is altered, e.g., temperature, external force, channels width, etc. Even when the density peaks weaken to nearly constant, this wavelength does not change.

The above results can be captured very well by the quasi-continuum model. Excluding the results for the very small density ($\rho^* = 0.321$), one can identify by $g_o \approx 0.9\sigma$ the wave length of the quasi-continuum theory. By fitting the d^2c/dz^2 as predicted by Eq. (56) (see Appendix 2) to MD calculations, we obtain the values of Ag_o for different channel widths, as shown in Fig. 4.

Figure 4a corresponds to the smallest channel studied ($h_{ch} = 0.9$ nm), Fig. 4b to $h_{ch} = 1.5$ nm and Fig. 4c to $h_{ch} = 2.7$ nm. In all cases, we have $n = 1$. Equation (42) can now be used in order to extract the g_o value for the quasi-continuum model. We mentioned before that if we know any two of h_{ch}, g_o and A, we can estimate the third one, provided we can estimate the integer n. The results are shown in Table 1, and the accuracy of the quasi-continuum model seems to be very good.

Numerical integration of d^2c/dz^2 and symmetry condition give

$$c(z) = c(z = 0) + c_2 \int {}_1F_1 dz. \tag{45}$$

Now, we can plot the results for $c(z)$ in Fig. 5a–c. Figure 5a is analogous to the MD extracted density profile for the $h_{ch} = 0.9$ nm channel. Calculations for the $h_{ch} = 1.5$ nm channel are presented in Fig. 5b. Here, the density peak oscillation is not so obvious, but still this is close to the respective MD extracted profile. Interesting results come from the $h_{ch} = 2.7$ nm channel, where the similarity with MD simulation density profile is clear.

One could observe that the variation of D along the channel width plays the most important role in explaining the uneven peaks observed by the NEMD calculations. Strong curvatures of the $D(z)$ result in high local peaks of $c(z)$.
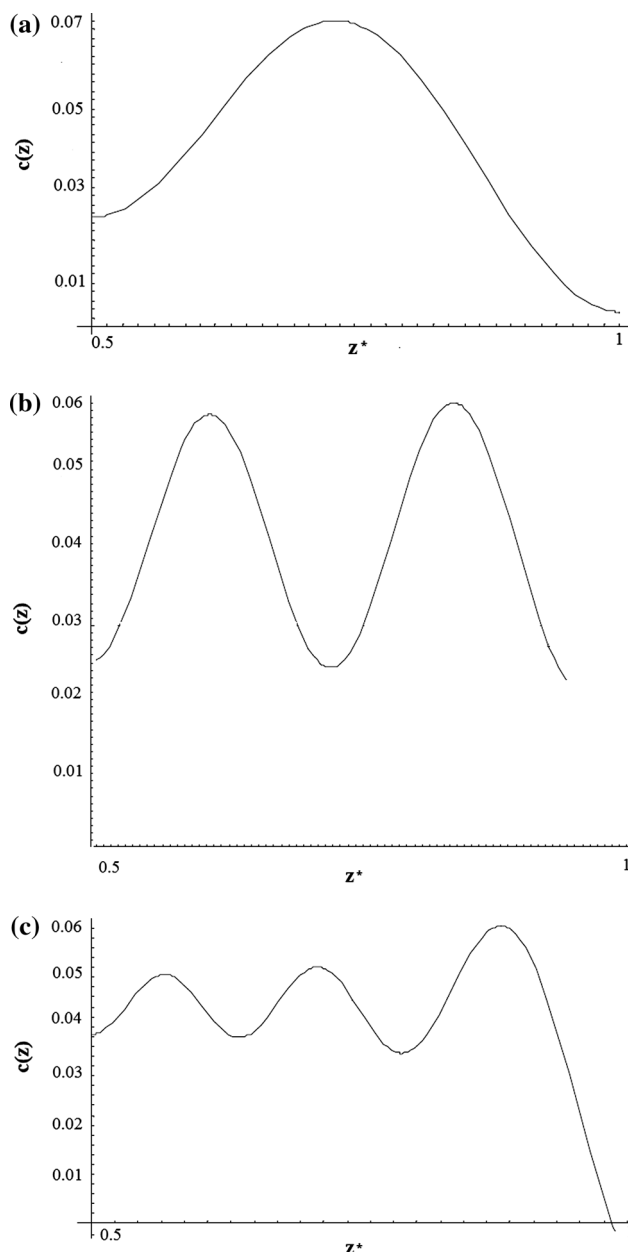
Fig. 5 Numerical integration of d^2c/dz^2 shown in Fig. 4. The results scale with the density profile at $z^* = 0.5$ (*middle of the channel*) found by molecular dynamics of Fig. 3. The coordinate scales with 0.2 g_o ($g_o = 0.3$ nm). **a** $Ag_o = 0.12$ and $h_{ch} = 0.9$ nm, $0.025 + \frac{0.045}{2F}$ (average = 0.0385), **b** $Ag_o = 0.045$ and $h_{ch} = 1.5$ nm, $0.025 + \frac{0.035}{2.1F}$ (average = 0.0420) and **c** $Ag_o = 0.024$ and $h_{ch} = 2.7$ nm, $0.0384 + \frac{0.00375}{6.2F}$ (average = 0.0428)

5 Conclusions

We have presented a quasi-continuum self-diffusion approach which is able to reproduce results from non-equilibrium molecular dynamics simulations of planar

Poiseuille liquid argon nanoflow. If diffusion coefficient values are known, in addition with a micro structural internal length, g, the model can predict the ordering effects caused by atomic-scale flow conditions. In nanoflows, the effect of system temperature, applied driving force, wall spring constant, wall–fluid interaction ratio and average fluid density on the distribution of fluid density becomes important, leading to behavior different than expected from classical continuum theory.

MD simulations reveal strong fluid ordering through number density profiles for $h_{ch} \leq 2$ nm, while for $h_{ch} \geq 2$ nm profiles are uniform in most of the core channel area but ordering persists very close to the wall. Fluid ordering near the wall increases when system temperature decreases, the spring constant (wall stiffness) increases, wall hydrophilicity increases, and average fluid density decreases, while external forces do not affect number density profiles significantly.

To capture the MD calculated fluid distribution densities, we constructed a quasi-continuum model for the self-diffusion equation. This model was based on the concept of the spinodal decomposition of solid diffusion. A characteristic length g appeared in the new differential equation that gives rise to oscillations in the steady state distribution of the fluid atoms. Furthermore, a wave number g/h_{ch} can be constructed using the channel width h_{ch}. It is found that the inhomogeneity of the diffusion coefficient plays a significant role in the details of the fluid density distribution by exponentially decreasing the peaks of the density oscillations close to the channel boundaries. In this way, the fluid–wall interaction is fully introduced in the quasi-continuum approach. The resulting quasi-continuum equation is of Schrodinger type and a "quantum" condition can be formulated, connecting g, h_{ch} and $\partial^2 D/\partial z^2$.

Either the atomistic model or the quasi-continuum model presented in this work seems capable of reproducing the Poiseuille nanoflow characteristics regarding the ordering of the fluid in the channel. Of particular, importance is the inhomogeneity of the diffusion coefficient in capturing the density profiles with the quasi-continuum theory. The variation of the diffusion coefficient across the channel width (decreasing toward the channel walls) is related to wall smoothness.

The only shortcoming of the present scheme is that it necessitates an MD simulation realization in order to extract fluid parameters (diffusion coefficient variation and characteristic length g). However, if one has to simulate a complex flow domain, consisting of various channel parts to be simulated by fully atomistic MD methods, it would require extensive computational resources. In the frame of the proposed scheme, all parts could be modeled using the quasi-continuum model. We emphasize that the same equations can be employed in a multi-scale problem covering length scales from nano to macro.

Appendix 1: ODE solution for the 1D state problem

The general solution of Eq. (30) is

$$c(z) = A_1 + A_2 z + A_3 \sin \frac{z}{g} + A_4 \cos \frac{z}{g} \qquad (46)$$

where $A_1, \ldots A_4$ are constants to be determined by BC. The first two terms are similar to the classic solution. The other two terms are the non-classic part of the solution. Taking the region $0 \leq z \leq h_{ch}$, (h_{ch} is the channel width), we impose the following BCs that are compatible with the Poiseuille flow in the normal to z-direction.

$$J = -D\left(\frac{dc}{dz} + g^2 \frac{d^3 c}{dz^3}\right) \qquad (47)$$

At $z = 0$ and h_{ch}, $J = 0$, that is no flux at the walls, which gives

$$A_2 = 0 \qquad (48)$$

At $z = h_{ch}/2$, $c = c_o$ a datum point at the middle of the channel (can be thought of as a constant that increases with temperature), which gives

$$A_1 = c_o - A_3 \sin \frac{h_{ch}}{2g} - A_4 \cos \frac{h_{ch}}{2g}, c_o \geq 0 \qquad (49)$$

Symmetry of the concentration implies $dc/dz = 0$ at $z = h_{ch}/2$, which gives

$$A_3 \cos \frac{h_{ch}}{2g} = A_4 \sin \frac{h_{ch}}{2g} \tag{50}$$

This condition implies that $J = 0$ at $z = h_{ch}$, as expected. It can be shown that $J = 0$ for all z, $0 \leq z \leq h_{ch}$.

Mass conservation implies

$$\int_0^{h_{ch}/2} c(z)\mathrm{d}z = \bar{c}\frac{h_{ch}}{2}, \quad \bar{c} > 0 \tag{51}$$

which gives

$$A_1 + A_4 \frac{2g}{h_{ch}} \sin \frac{h_{ch}}{2g} + A_3 \frac{2g}{h_{ch}} \left(1 - \cos \frac{h_{ch}}{2g}\right) = \bar{c} \tag{52}$$

Solving Eqs. (49), (50) and (52), we obtain

$$A_4 = (c_o - A_1) \cos \frac{h_{ch}}{2g} \tag{53}$$

$$A_3 = (c_o - A_1) \sin \frac{h_{ch}}{2g} \tag{54}$$

$$A_1 = c_o \frac{\frac{\bar{c}}{c_o} - \frac{2g}{h_{ch}} \sin \frac{h_{ch}}{2g}}{1 - \frac{2g}{h_{ch}} \sin \frac{h_{ch}}{2g}} \tag{55}$$

For $\bar{c} = c_o$, we obtain the classic relation $c = c_o$.

Appendix 2: Asymptotic analysis

The solution of Eq. (37) can be written as combinations of hypergeometric function $_1F_1$ and the Hermitian polynomial H:

$$\frac{\mathrm{d}^2 c}{\mathrm{d}z^2} = e^{-\frac{Az^2}{2g_0}} \left\{ c_1 H\left(\frac{1 - Ag_o}{2Ag_o}, \frac{\sqrt{A}z}{\sqrt{g_o}}\right) + c_2 \, _1F_1\left(\frac{-1 + Ag_o}{4Ag_o}; \frac{1}{2}; \frac{Az^2}{g_o}\right) \right\} \tag{56}$$

where c_1 and c_2 are real constants. Note that only the hypergeometric function $_1F_1$ is symmetric with respect to z. Therefore, symmetric cases are accepted only if $c_1 = 0$. An interesting expansion of the solution around $z = 0$ (middle of the channel) is given below. In some cases in the field of heat transfer, the variational iteration method is utilized as an approximate analytical method to overcome some inherent limitations arising as uncontrollability to the nonzero endpoint boundary conditions (see, for example, Fouladi et al. 2010).

It is of interest to expand the symmetric solution ($c_1 = 0$) around point $z = 0$ (the middle of the channel width).

$$\frac{\mathrm{d}^2 c}{\mathrm{d}z^2} = e^{-\frac{Az^2}{2g_o}} c_2 {}_1F_1\left(\frac{-1 + Ag_o}{24g_o}; \frac{1}{2}; \frac{Az^2}{g_o}\right)$$
$$\approx c_2 \left\{ 1 - \frac{z^2}{2g_o^2} + \left(\frac{1}{24g_o^4} + \frac{A^2}{12g_o^2}\right)z^4 \right.$$
$$\left. - \left(\frac{1}{720g_o^6} + \frac{7A^2}{360g_o^2}\right)z^6 + 0(z^8) \right\} \tag{57}$$

Note that the expansion (57) involves only even powers of z. Taking the conditions $dc/dz = 0$ and $c = c_o$ at $z = 0$, and retaining the first two terms of (57), we obtain

$$\frac{\mathrm{d}c}{\mathrm{d}x} \approx c_2 \left(z - \frac{z^3}{6g_o^2}\right) + 0(z^5) \tag{58}$$

and

$$c \approx c_o + c_2 \left(\frac{z^2}{2} - \frac{z^4}{24g_o^2}\right) + 0(z^6) \tag{59}$$

Assuming that (59) should provide $c \geq 0$ for all values of $c_o \geq 0$, we conclude that $c_2 \geq 0$. In other words, $dc^2/dz^2 \geq 0$ at $z = 0$, a result that is verified by the NEMD calculations!

Appendix 3: Diffusion for asymmetric wall conditions

The case of asymmetric wall conditions can be studied by a diffusion inhomogeneous distribution of the type

$$D = D_o(1 - Bz/g_o) \tag{60}$$

The diffusion equation becomes

$$\frac{d^4 c}{\mathrm{d}z^4} + \frac{(1 - Bz/g_o)}{g_o^2} \frac{d^2 c}{\mathrm{d}z^2} = 0 \tag{61}$$

The solution of Eq. (61) can be put in closed form.

$$\frac{d^2 c}{\mathrm{d}z^2} = c_2 A_i \left[\frac{-1 + Bz/g_o}{B^{2/3}}\right] + c_3 B_i \left[\frac{-1 + Bz/g_o}{B^{2/3}}\right] \tag{62}$$

where A_i and B_i are Airy functions and c_2, c_3 are constants. The full solution of Eq. (62) is given by

$$c(z) = c_o + c_1 z + c_2 C_A(z) + c_3 C_B(z) \tag{63}$$

where c_o, c_1, c_2, c_3 are constants.

The general form of the functions $C_A(z)$ and $C_B(z)$ are

$_pF_q$ is the generalized hypergeometric function, I is the modified Bessel function of the first kind, Γ is the Gamma function, and B is a parameter of the problem.

We believe that the chemical affinity between the walls and the fluid, as well as the roughness of the walls, influence the diffusion coefficient distribution and this, in turn, affects the steady state concentration profiles.

$$C_A(z) = \frac{1}{3^{11/3}\Gamma\left(\frac{4}{3}\right)\Gamma\left(\frac{5}{3}\right)} \left\{ 3\left(-\frac{g_o}{B}+z\right)^2 \Gamma\left(\frac{1}{3}\right) {}_pF_q\left[\left\{\frac{1}{3}\right\}, \left\{\frac{4}{3},\frac{5}{3}\right\}, \frac{B\left(-\frac{g_o}{B}+z\right)^2}{9g_o^2}\right] \right.$$

$$-\frac{1}{B}\left[3^{1/3}\left(\frac{B}{g_o^3}\right)^{1/3}\Gamma\left(\frac{2}{3}\right)\left[6g_o^2 - 3^{1/3}2g_o^2\left(\frac{\sqrt{B}\left(-\frac{2}{B}+z\right)^{3/2}}{g_o^{3/2}}\right)^{2/3} I\left[-\frac{2}{3}, \frac{2\sqrt{B}\left(-\frac{g_o}{B}+z\right)^{3/2}}{3g_o^{3/2}}\right]\Gamma\left(\frac{1}{3}\right)\right.$$

$$\left.\left.\left. + 3B\left(-\frac{g_o}{B}+z\right)^3 {}_pF_q\left[\left\{\frac{2}{3}\right\}, \left\{\frac{4}{3},\frac{5}{3}\right\}, \frac{B\left(-\frac{g_o}{B}+z\right)^2}{9g_o^2}\right]\right]\right]\right\} \tag{64}$$

$$C_B(z) = \frac{1}{3^{17/6}\Gamma\left(\frac{4}{3}\right)\Gamma\left(\frac{5}{3}\right)} \left\{ 3^{2/3}\left(-\frac{g_o}{B}+z\right)^2 \Gamma\left(\frac{1}{3}\right) {}_pF_q\left[\left\{\frac{1}{3}\right\}, \left\{\frac{4}{3},\frac{5}{3}\right\}, \frac{B\left(-\frac{g_o}{B}+z\right)^2}{9g_o^3}\right] \right.$$

$$+\frac{1}{B}\left[\left(\frac{B}{g_o^3}\right)^{1/3}\Gamma\left(\frac{2}{3}\right)\left[6g_o^2 - 3^{1/3}2g_o^2\left(\frac{\sqrt{B}\left(-\frac{g_o}{B}+z\right)^{3/2}}{g_o^{3/2}}\right)^{2/3} I\left[-\frac{2}{3}, \frac{2\sqrt{B}\left(-\frac{g_o}{B}+z\right)^{3/2}}{3g_o^{3/2}}\right]\Gamma\left(\frac{1}{3}\right)\right.$$

$$\left.\left.\left. + 3B\left(-\frac{g_o}{B}+z\right)^3 {}_pF_q\left[\left\{\frac{2}{3}\right\}, \left\{\frac{4}{3},\frac{5}{3}\right\}, \frac{B\left(-\frac{g_o}{B}+z\right)^3}{9g_o^3}\right]\right]\right]\right\} \tag{65}$$

Appendix 4: Temperature profile

Temperature is calculated in each bin across the channel using

$$T_{\text{bin}} = \frac{m_{Ar}}{3N_{\text{bin}}k_B} \sum_{n-1}^{N_{\text{bin}}} \sum_{i-1}^{3} \left(v_{n,i} - \bar{v}_i\right)^2 \tag{66}$$

where N_{bin} is the number of fluid atoms in the bin examined, $i = 1, 2, 3, \ldots$ denotes the x, y, z component of the atomic velocity v_{n-1}, $\bar{v}_i$ is the ith component of the mean

macroflow velocity, k_B is the Boltzman constant, and m_{Ar} is argon atom mass.

In Fig. 6a, the calculated fluid temperature distribution for $h_{\text{ch}} = 6.3$ nm is presented. We can see that for each system temperature (the temperature value imposed at the wall's thermostats, 100, 120, or 150 K), the temperature profile is approximately flat at this temperature value. We obtain similar flat behavior when we vary system parameters such as channel width h_{ch}, the wall atoms spring constant K^*, the wall–fluid interaction ratio $\varepsilon_{wall}/\varepsilon_{fluid}$ an the
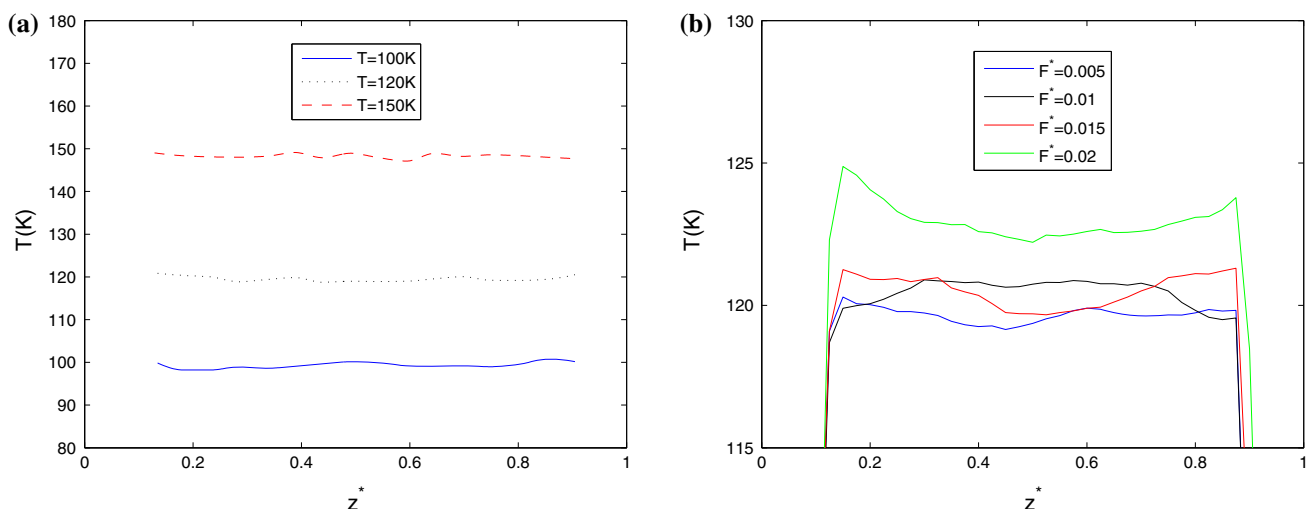

Fig. 6 Temperature profiles a for system temperature $T = 100$, 120 and 150 K, and $h_{\text{ch}} = 6.3$ nm b for various magnitudes of the F_{ext} (normalized), $T = 120$ K and $h_{\text{ch}} = 17.1$ nm

average fluid density ρ^*. However, in Fig. 6b, for $h_{ch} = 17.1$ nm and external forces above 0.036 pN, temperature profiles are not uniform and show a rise in the middle of the channel and near the solid walls. Similar behavior is reported on Nagayama and Cheng (2004) when the external force that drives the flow becomes large. We attribute this behavior to the fact that at large channel widths, in combination with external forces of large magnitude, strain rates inside the nanochannel increase, and the system has non-linear response.

References

Allen MP, Tildesley TJ (1987) Computer simulation of liquids. Clarendon Press, Oxford

Asproulis N, Drikakis D (2011) Wall-mass effects on hydrodynamic boundary slip. Phys Rev E 84:031504

Binder K, Horbach J, Kob W, Paul W, Varnik F (2004) Molecular dynamics simulations. J Phys: Condens Matter 16:429–453

Cahn JW (1961) On spinodal decomposition. Act Meta 9:765–801

Cahn JW, Hilliard JE (1958) Free energy of a non uniform system. I. Interfacial free energy. J Chem Phys 28:258–267

Cahn JW, Hilliard JE (1959) Free energy of a non uniform system. III. Nucleation in a two-component incompressible fluid. J Chem Phys 31:688–699

Cook HE (1970) Brownian motion in spinodal decomposition. Act Meta 18:297–306

Courant R, Hilbert D (1953) Methods of mathematical physics, vol I. Wiley Interscience, New York

Crank J (1975) The mathematics of diffusion. Oxford University Press, New York

Darken LS (1948) Diffusion, mobility and their interrelation through free energy in binary metallic systems. Trans AIME 175:184–201

Evans DJ, Holian BL (1985) The Nosé–Hoover thermostat. J Chem Phys 83:4069–4074

Fouladi F, Hosseinzadeh E, Barari A, Dmairry G (2010) Highly nonlinear temperature-dependent fin: analysis by variational iteration method. Heat Tranfer Res 41:1–11

Gini-Castagnoli G, Ricci FP (1960) Self-diffusion in liquid argon. J Chem Phys 32:19–20

Hartkamp R, Ghosh A, Weinhart T, Luding S (2012) A study of the anisotropy of stress in a fluid confined in a nanochannel. J Chem Phys 137:044711

Holian BL, Voter AF (1995) Thermostatted molecular dynamics: How to avoid the Toda demon hidden in Nosé–Hoover dynamics. Phys Rev E 52:2338–2347

Iwai Y, Uchida H, Koga Y, Arai Y, Movi Y (1996) Monte Carlo simulation of solubilities of aromatic compounds in supercritical carbon dioxide by a group contribution site model. Ind Eng Chem Res 35:3782–3787

Li Q, Liu C (2012) Molecular dynamics simulation of heat transfer with effects of fluid–lattice interactions. Int J Heat Mass Trans 55:8088–8092

Lipowsky R, Fisher ME (1986) Wetting in random systems. Phys Rev Lett 56:472–475

Lipowsky R, Huse DA (1986) Diffusion-limited growth of wetting layers. Phys Rev Lett 57:353–356

Marko JF (1993) Influence of surface interactions on spinodal decomposition. Phys Rev E 48:2861–2879

Nagayama G, Cheng P (2004) Effects of interface wettability on microscale flow by molecular dynamics simulation. Int J Heat Mass Trans 47:501–513

Priezjev NV (2007) Effect of surface roughness on rate-dependent slip in simple fluids. J Chem Phys 127:144708

Prigogine I, Glansdorff P (1965) Variational properties and fluctuation theory. Physica 31:1242–1256

Sofos F, Karakasidis TE, Liakopoulos A (2009a) Non-equilibrium molecular dynamics investigation of parameters affecting planar nanochannel flows. Cont Eng Sci 2:283–298

Sofos F, Karakasidis TE, Liakopoulos A (2009b) Transport properties of liquid argon in krypton nanochannels: anisotropy and non-homogeneity introduced by the solid walls. Int J Heat Mass Trans 52:735–743

Sofos F, Karakasidis TE, Liakopoulos A (2012) Surface wettability effects on flow in rough wall nanochannels. Microfluid Nanofluid 12:25–31

Somers SA, Davis HT (1991) Microscopic dynamics of fluids confined between smooth and atomically structured solid surfaces. J Chem Phys 96:5389–5407

Stanley HE (1971) Introduction to phase transitions and critical phenomena. Clarendon, Oxford

Thomas JA, McGaughey AJH (2007) Effect of surface wettability on liquid density, structure, and diffusion near a solid surface. J Chem Phys 126:034707

Voronov RS, Papavassiliou DV, Lee LL (2006) Boundary slip and wetting properties of interfaces: correlation of the contact angle with the slip length. J Chem Phys 124:204701